Discrete element method-generated data enhance CNN-based stress field prediction accuracy and efficiency in unidirectional fibre-reinforced polymer composites

Siyu Zhao [a], Xiaoxuan Ding [b], Jianqiao Ye [a], Xiaonan Hou [a,*]

[a] Department of Engineering, Engineering Building, Lancaster University, Lancaster, LA1 4YW, UK

[b] Department of Engineering Mechanics, College of Pipeline and Civil Engineering, China University of Petroleum, Qingdao, 266580, Shandong, China

[*] Corresponding author. Email address: x.hou@lancaster.ac.uk; Tel: +44 (0)1524 594826

Abstract

Accurate analysis of mechanical fields, such as stresses, strains, and deformation fields, is essential in the design and repair of composite materials. Compared to the time-consuming computational micromechanics methods, there is a high demand for developing a fast, efficient and accurate surrogate model to conduct mechanical fields analysis. This paper introduces a CNN-based U-Net model, mapping the stiffness distribution of unidirectional fibre-reinforced polymer composite laminae to their corresponding linear and nonlinear stress fields. The model is based on a dataset generated through discrete element method (DEM) simulations, which includes the simulation results from 50 representative volume elements with 60% fibre volume fraction and 50 with 40% fibre volume fraction for training, and 50 for each fibre volume fraction (60%, 50%, 40% and 30%) for testing. In comparison with existing studies, the proposed U-Net model, trained on DEM-generated data, demonstrates superior accuracy and efficiency in predicting both linear and nonlinear stress fields of laminae, including those with fibre volume fractions different from the training data, without requiring a large training dataset.

Keywords: Machine learning; Surrogate modelling; Discrete element method; Stress field prediction; Fibre-reinforced polymer composites.

1. Introduction

In recent years, fibre-reinforced polymer (FRP) composite laminates have been widely used across various engineering sectors owing to their exceptional physical and mechanical properties [1-7]. However, the inherently complex micro-geometrical structure of the composite gives rise to highly heterogeneous mechanical behaviour governed by multiple interacting factors, which limits its industrial applicability and poses significant challenges for design and repair [8-9]. Consequently, accurate prediction of the mechanical responses of FRP composite laminates, together with the establishment of reliable structure–property relationships, is of critical importance.

Analytical approaches based on the formulation of partial differential equations, together with experimental tests, are common methods for investigating the mechanical properties of FRP composite laminates [10-15]. However, these solutions are typically restricted to specific geometry, boundary and loading conditions, while experimental methods are cost-inefficient and often struggle to accurately simulate realistic service environments and loading scenarios. As a reliable alternative, physics-based computational numerical modelling, including the finite element method (FEM), discrete element method (DEM), and other similar techniques, has expanded the range of solvable problems and enabled high-fidelity modelling with lower demands on experimental setups [16-18]. Despite the high prediction accuracy of these methods, their intensive computational costs still limit the performance, particularly when numerous structure-property relationships must be rapidly identified to select optimal materials for industrial applications. Therefore, developing machine learning approaches as surrogate models that reduce computational time while maintaining prediction accuracy has attracted increasing interests in recent years [19-21].

Machine learning methods have shown a robust ability to extract complex relationships between input and output features across different subject domains [22-24]. For the identification of features along the structure-property chain, which is essential in the field of material science, ML methods have been widely utilized to predict homogenized mechanical properties [25-34]. However, extending ML approaches to the prediction of full field distribution properties is more challenging, as the prediction targets increase from a single quantity to a combination of several correlated quantities. To address this challenge, various deep learning architectures, such as fully connected neural network (FCNN), physics-informed neural network (PINN), graph neural network (GNN), convolutional neural network (CNN), among others, have been proposed and have achieved high accuracy [35-39]. In particular, image-based machine learning models have been extensively explored, in which both inputs and outputs are typically pixelated images generated through FEM analysis, representing the microstructures and corresponding mechanical field distributions of the studied materials, respectively. Nie et al. [40] introduced a novel convolutional neural network framework called StressNet, in which geometry, load and boundary conditions are taken as separate input channels to predict the linear stress fields in 2D cantilevered structures. Frankel et al. [41] proposed the ConvLSTM architecture to improve effectiveness in predicting the elastic-plastic stress fields of polycrystals. This approach employed a hybrid neural network design combining convolutional neural network with long short-term memory, effectively extracting both spatial and temporal information from the data. Khanolkar et al. [42] studied the elastic strain fields in additively produced microstructures containing defects of various shapes by using an image colorization algorithm. Croom et al. [43] investigated the distribution of elastic stress fields in additively manufactured metals through a modified U-Net style CNN model and demonstrated that the U-Net based model achieved better accuracy compared to the StressNet and the image colorization algorithm previously proposed in the literature.

More recently, surrogate modelling of full-field distribution properties of composites has received increased attention. Feng et al. [44] utilized a difference-based neural network (DiNN) to conduct stress analysis of heterogeneous materials including composites. Instead of directly mapping the microstructure to the stress field distribution of the material, this method focused on predicting the differences in stress distributions resulting from varying input features. Yang et al. [45] developed an end-to-end conditional adversarial neural network model to predict the stress and strain fields in composites, achieving excellent accuracy regardless of component shapes, boundary conditions and geometrical complexity. Bhaduri et al. [46] applied a U-Net architecture-based model to bridge the gap between the microstructures of fibre-reinforced matrix composite materials and their corresponding von Mises stress fields, and utilized transfer learning to train the model, enabling accurate prediction of the stress fields for systems containing larger numbers of fibres while significantly reducing the required training dataset size. Subsequently, by incorporating transformer mechanisms into the network architecture, Peng et al. [47] proposed a 3D TransU-Net model integrated with transfer learning strategy to predict the stress fields of fibre-reinforced composites under various fibre volume fractions and loading paths. Li et al. [48] employed a U-Net deep learning model embedded with the Triplet Attention mechanism to enhance the prediction of nonlinear stress fields in unidirectional CFRP composites with microvoids. In addition, a series of novel architectures, such as neural operator-based and sequence-based models, have also been explored [49-50]. To further reduce training costs of machine learning models, Xu et al. [51] introduced the SuperMeshingNet, a network that directly projects low mesh-density mechanical fields, which are cheaper to train, to high-resolution mechanical fields. Yacouti et al. [52] developed a novel network structure called CompINet, integrating the advantages of convolutional neural network and graph neural network, which achieved high accuracy in predicting linear and nonlinear stress fields while requiring twenty times less data compared to the existing data-driven methods.

While machine learning models based on FEM-generated binary pixel images have been employed as accurate and fast surrogate models for studying mechanical field distribution of composites, they typically require large training datasets, often ranging from 500 to 2000 samples, to achieve good generalization [53-54]. Moreover, these models suffer from an obvious decrease in prediction accuracy as the complexity of the task increases. As shown in [52], the CompINet model achieved a mean R^2 value of 0.965 for the stress field prediction in the linear elastic stage, but the value dropped to 0.845 when the material entered the nonlinear plastic stage. Therefore, there is a strong need to explore the integration of machine learning with alternative numerical modelling approaches, and the incorporation of more physically informed features into the training process, to address these issues and enhance surrogate modelling.

As an alternative to FEM, DEM has proven effective in simulating both the mechanical field distributions and the failure patterns of composites [18,55,56]. In this work, a CNN-based U-Net model trained on DEM-generated data is introduced to predict both linear and nonlinear stress fields of unidirectional (UD) FRP composite laminae. Compared with FEM-generated binary pixel images, the DEM-generated data used for model training offer several advantages. First, based on the DEM-generated data, bond stiffness distribution maps are constructed as inputs and stress field maps as outputs, thereby preserving the local bond-level information and global force-chain patterns in the composite microstructure. Second, in a DEM model, the material domain is discretized into interacting particles, and the stress and deformation of the entire material are obtained by tracing the behavior of individual particles. Given that the particle behavior in DEM is predominantly governed by interactions with neighboring particles, the resulting stress fields exhibit strong spatial correlations at the neighborhood scale. CNN-based models, with their localized receptive fields and hierarchical feature extraction, offer distinct advantages in capturing these spatially correlated patterns from DEM-generated data, thereby enhancing the models' fitting and generalization capabilities.

In summary, the main contributions and application areas of this study are as follows:

(1) A calibrated DEM model is developed to obtain stress field distributions of UD FRP composite laminae under transverse tension loads, considering different fibre volume fractions and spatial distributions.

(2) A novel surrogate modelling framework of stress field is proposed, integrating DEM-generated data with a CNN-based U-Net architecture to achieve data-efficient and robust prediction of linear and nonlinear stress fields from stiffness distributions.

(3) Extensive numerical validations are conducted to evaluate the performance of the proposed framework, extending testing beyond the training distribution to unseen fibre volume fractions and spatial distributions, and benchmarking against a conventional U-Net model trained on FEM-generated data.

(4) The proposed framework provides a low-computational-cost method that offers essential insights into both the homogenization process in design calculations and localized phenomena in UD FRP composite laminates, such as stress concentrations and failure patterns. Owing to its accuracy and data-efficiency, the framework shows strong potential for integration into digital twin systems and additive manufacturing-driven design and repair processes, enabling rapid informed decision-making.

The remainder of this paper is organized as follows. Section 2 presents the methodology employed to predict the stress field in UD FRP composite laminates under transverse tension loads. Section 3 provides comprehensive numerical validation results. Finally, Section 4 concludes the paper.

2. Methodology

2.1. Basic notations and definitions

In this work, the stress field of an UD FRP composite lamina under transverse tension loads is considered. The lamina is assumed to consist of two constituent phases, namely the matrix and the fibre. The superscripts m and f are used as phase labels for the matrix

and fibre, respectively, and f^{m} and f^{f} denote the corresponding matrix and fibre volume fractions, which are scalar parameters satisfying

$$f^{\mathrm{m}} + f^{\mathrm{f}} = 1. \tag{1}$$

The reference configuration of the lamina is defined as $\Omega \subset \mathrm{R}^2$. The domain Ω can be decomposed into two non-overlapping subdomains corresponding to the matrix domain Ω^{m} and fibre domain Ω^{f}, such that $\Omega^{\mathrm{m}} \cup \Omega^{\mathrm{f}} = \Omega$ and $\Omega^{\mathrm{m}} \cap \Omega^{\mathrm{f}} = \emptyset$.

The configuration of the lamina is characterized by a set of descriptors denoted by M, which can be written as:

$$M = \left\{ f^{\mathrm{f}}, A, L \right\}. \tag{2}$$

where f^{f} is the fibre volume fraction, A is the fibre spatial distribution within the domain Ω, and L represents the loading condition. The stress field of the lamina is denoted by $\sigma(x), x \in \Omega$. Accordingly, the mapping from the lamina configuration M to the corresponding stress field $\sigma(x)$ can be expressed as:

$$\sigma(x) = G(M)(x). \tag{3}$$

where G denotes the nonlinear mapping operator.

2.2. DEM model development

A 2D plane strain computational micromechanics DEM model is employed in Particle Flow Code software package (PFC 2D) to investigate the stress field distribution of UD FRP composite laminae under transverse tension loads. Within the DEM model, the material domain Ω is discretized into bonded particles. The contact forces between interacting particles are determined from their overlap and relative motions based on the force–displacement law, and the positions of particles over a time step Δt are governed by Newton's second law, which can be defined as:

$$\text{Translational motion} \quad F_i = m(\ddot{x}_i - g_i). \tag{4}$$

$$\text{Rotational motion} \quad M_3 = I\dot{\omega}_3. \tag{5}$$

where $i = 1, 2$ denotes the components in the *x*- and *y*-coordinate directions, respectively, F_i is the resultant force, *m* and $\ddot{x}_i$ are the mass and the acceleration of the particle, respectively, g_i is the body force acceleration vector, M_3 is the out of balance moment in the z-coordinate direction, $\dot{\omega}_3$ is the angular acceleration in the z-coordinate direction, and *I* is the rotational inertia of the particle.

The motion equations in Eqs. (4)-(5) are solved using a central finite difference algorithm. First, the translational and rotational accelerations $\ddot{x}_i$ and $\dot{\omega}_3$ at time *t* are calculated as:

$$\ddot{x}_i(t) = \frac{1}{\Delta t}\left(\dot{x}_i(t + \Delta t/2) - \dot{x}_i(t - \Delta t/2)\right). \tag{6}$$

$$\dot{\omega}_3(t) = \frac{1}{\Delta t}\left(\omega_3(t + \Delta t/2) - \omega_3(t - \Delta t/2)\right). \tag{7}$$

By inserting Eqs. (4)-(5) into Eqs. (6)-(7), the translational and rotational velocity at time $t + \Delta t/2$ can be calculated as:

$$\dot{x}_i(t + \Delta t/2) = \dot{x}_i(t - \Delta t/2) + \left(\frac{F_i(t)}{m} g_i\right)\Delta t. \tag{8}$$

$$\omega_3(t + \Delta t/2) = \omega_3(t - \Delta t/2) + \left(\frac{M_3(t)}{I}\right)\Delta t. \tag{9}$$

Finally, the position of the particle at time $t + \Delta t$ is updating by integrating velocities in Eqs. (8)-(9) and $F_i(t + \Delta t)$ and $M_3(t + \Delta t)$ are obtained through the application of the force-displacement law.

For the DEM model development in this work, a hexagonal arrangement is used for packing both matrix (blue color) and fibre (pink color) particles within a 50×50 μm representative volume element (RVE) of the lamina cross-section (as shown in Fig. 1). The method proposed in [57] is used to introduce randomness into the spatial fibre distribution corresponding to a specific fibre volume fraction. After the composite lamina RVE with a random spatial fibre distribution is generated, a constant tensile

velocity of $5\ \mathrm{mm/s}$ is applied simultaneously to the particles on the left- and right-hand edges of the RVE to examine its transverse mechanical responses.

Within the developed DEM model, three types of contact bonds are developed to connect each group of particles: the parallel-bond between fibre particles, the parallel-bond between matrix particles and the soft-bond between fibre and matrix particles (as illustrated in Fig. 1). The parallel-bond and soft-bond are both built-in contact bond models in the PFC package, which behave like a set of elastic springs with constant normal and shear stiffness, uniformly distributed over the rectangular cross-section lying on the contact plane and centered at the contact point. The main difference between them is that if the maximum normal stress acting on the bond exceeds its tensile strength, the soft-bond may enter into a softening regime instead of being removed if it is a parallel-bond. More details about the parallel-bond and soft-bond can be found in [58].

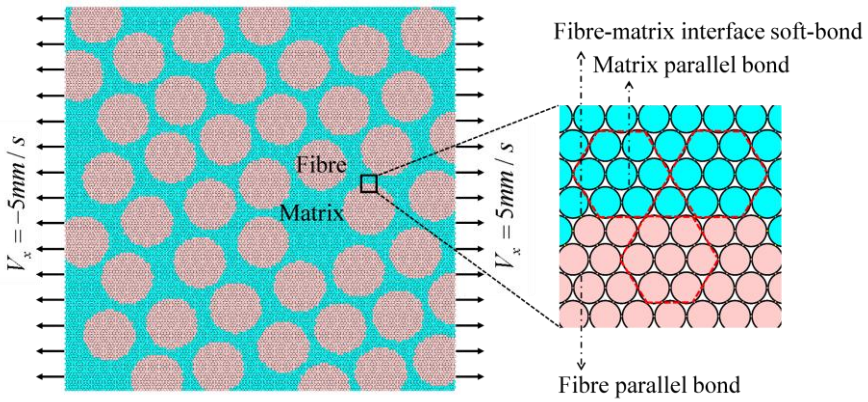

Fig. 1. An RVE sample of the DEM model under transverse tension loads.

The microscale parameters of the proposed DEM model are calibrated by the macroscopic material properties of each composite constituent. In this work, the material properties of the fibre, matrix and fibre-matrix interface for the UD FRP composite lamina are shown in Table 1. The calibration procedure for the three types of contact bonds follows the methods outlined in [23-24]: First, the contact stiffness is calculated using the explicit theoretical formulas with variables of the respective

Young's modulus and the Poisson's ratio of the fibre and matrix. The formulas are expressed as [60]:

$$k_n = \frac{2E\lambda}{2\sqrt{3}(1+v)}\left(1+\frac{2}{3(1-v)}\right), \tag{10}$$

$$k_s = \frac{2\left|(3v-1)\right|E\lambda}{6\sqrt{3}(1-v^2)}. \tag{11}$$

where k_n and k_s are the normal and shear contact stiffness, respectively, E is the elastic modulus of material, v is the Poisson's ratio of material, and λ is the particle thickness.

Second, the micro strength of the matrix bonds is obtained through a convergence study, which indicates that the micro strength of the material bonds is linearly related to the macro strength of the material, with a coefficient of 1.7. The micro strength of the fibre-matrix interface bonds is calculated using the Mohr-Coulomb criterion, which is defined as:

$$\sigma_{\mathrm{mt}} = 2c\frac{\cos(\alpha)}{1+\sin(\alpha)}. \tag{12}$$

where σ_{mt} is the matrix tensile strength, c is the cohesion yield stress, and α is the internal friction angle. In this work, $\sigma_{\mathrm{mt}} = 60$ Mpa and $\alpha = 15^{\circ}$ are used for the Mohr-Coulomb criterion. Therefore, the corresponding cohesion c is calculated as 39.1 MPa, which gives the fixed normal interface strength of 39.1 MPa.

Since fibre fracture is unlikely to occur during loading, the micro strength of the fibre bonds is set to a very high value to prevent bond breakage. Finally, the softening factor and the softening tensile strength factor for the fibre-matrix interface soft-bond are calibrated through trial-and-error methods and the determined micro parameters are validated through the results from experimental tests [23-24].

Table 1: Material properties of fibre, matrix and interface [59].

Fibre	Transverse modulus, E_{f} (Gpa)	40
	Poisson's ratio, v_{f}	0.25
Matrix	Modulus, E_{m} (Gpa)	4
	Poisson's ratio, v_{m}	0.35
	Tensile strength, σ_{mt} (Mpa)	60
Interface	Fracture energy, G (J/m^2)	10

2.3. U-Net model development

In this work, a U-Net model is employed to map the lamina configuration M to the corresponding stress field $\sigma(x)$. The U-Net architecture first compresses the input information through an encoder to extract hierarchical features, and then reconstructs the spatial resolution through a decoder, producing the target output of the stress field. This process can be expressed as:

$$E_l = f^l_{\text{encoder}}\left(E_{l-1};\theta\right), \quad l = 1, 2, \ldots, n, \tag{13}$$

$$D_l = f^l_{\text{decoder}}\left(\left[D_{l+1} \uparrow 2; E_l\right];\theta\right), \quad l = n-1, n-2, \ldots, 1, \tag{14}$$

$$Y = f_{\text{final}}\left(D_1;\theta\right). \tag{15}$$

where E_l and D_l are the encoder and decoder feature maps at the l-th spatial resolution level, $E_0 = \mathcal{M}$, which is the lamina configuration, f^l_{encoder} and f^l_{decoder} are the encoder and decoder blocks, respectively, θ is the learnable parameters, n is the depth of the network, $[\cdot;\cdot]$ denotes the channel-wise concatenation, $\uparrow 2$ represents spatial resolution doubling, and f_{final} is the final mapping layer that projects the decoder feature map D_1 to the predicted stress field Y.

2.3.1. Data pre-processing

The DEM-generated data for training and testing the U-Net model consist of a set of microstructures of UD FRP composite laminae with different fibre volume fractions and their corresponding stress field distributions. In the DEM simulations, the macro-mechanical responses are described in terms of the movement of each particle and the

inter-particle force acting at each contact bond. Therefore, the force distribution of contact bonds during the loading process is extracted as a representative of the stress field distribution of the lamina. In this work, the normal component of the force at each contact bond, defined in the local contact coordinate system, is selected as the target to evaluate the performance of the proposed U-Net model, as it dominates material strength and failure in the discrete element framework [61-62]. The shear force component could also be incorporated in a similar manner for training.

From the DEM modelling, the microstructure of each RVE can be represented by the stiffness distribution at contact bonds. On this basis, the mapping from the microstructure to the stress field is expressed as a mapping from the stiffness distribution to the stress field. In a sense, the DEM model provides a physically meaningful field-to-field mapping.

The stiffness distribution and stress field provided at the contact bond level from the DEM model are transformed into a uniform grid for U-Net model training and prediction. To preserve the resolution of each bond, the grid division must ensure that a grid cell can only be occupied by at most one contact bond. Therefore, a 512×512 grid division is generated, and the contact bonds are assigned to the grids according to their relative positions (as shown in Fig. 2). In addition, a grid resolution sensitivity study has been conducted using a resolution of 256×256. The results indicate that the proposed model maintains robust and accurate predictions across different grid resolutions. Considering the need to avoid information loss while also preventing unnecessary increases in computational cost, the 512×512 grid division is considered suitable. Accordingly, The input for the U-Net model becomes the stiffness distribution in a 512×512 grid containing normal stiffness values, which are k_{fibre}, k_{matrix}, and $k_{\mathrm{interface}}$ for fibre parallel-bonds, matrix parallel-bonds, and fibre-matrix interface soft-bonds, respectively (as shown in Fig. 3(a)). The output corresponds to the stress field in a 512×512 grid containing the normal component of bond force values,

which are σ_{fibre}, σ_{matrix}, and $\sigma_{\text{interface}}$ for the same three types of contact bonds (as shown in Fig. 3(b)).

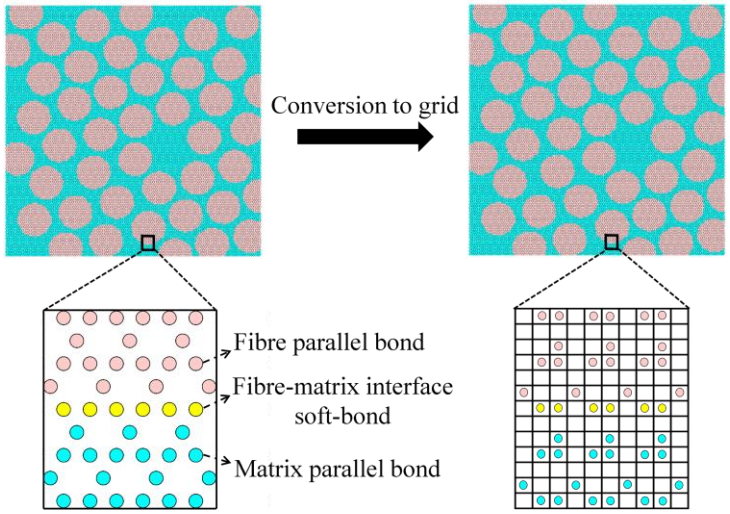

Fig. 2. Conversion of DEM-generated contact bonds to a uniformly spaced 512×512 grid.

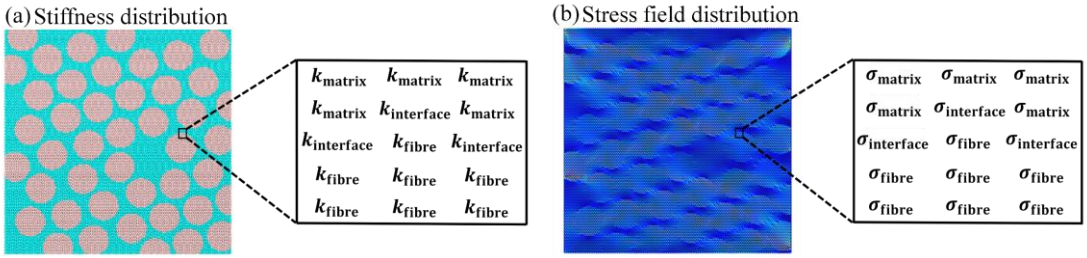

Fig. 3. A 512×512 grid is used to represent (a) the stiffness distribution of the lamina or (b) the stress field distribution of the lamina.

2.3.2. Framework of the predictive model

The framework of the predictive model used in this work is shown in Fig. 4. First, the contact bond-based stiffness distribution from the DEM model is transformed into a uniform 512×512 grid through bond-to-grid mapping. The grid-based stiffness distribution is then fed into the U-Net model, whose encoder consists of six repeating contracting blocks. Every block consists of two 3×3 2D convolutions with padding 1, each followed by an instance normalization and a ReLU operation. A 2×2 max

pooling operation with stride 2 is used between the successive contracting blocks to reduce the grid size. At each contracting step, the number of feature channels is doubled. Simultaneously, 6 repeating expansive blocks are built for the decoder. A 2×2 up-convolution operation with stride 2 is used for upsampling between blocks and to halve the number of feature channels. Skip connections are employed to concatenate the feature maps from each expansive block with the corresponding feature maps from the contracting block. Two 3×3 2D convolutions with padding 1, each followed by instance normalization and a ReLU activation, are used in each expansive block, which helps in feature extraction and refinement after upsampling. At the final layer, a 1×1 convolution is used to map the $64 \times 512 \times 512$ decoder output to a $1 \times 512 \times 512$ form with a single feature channel. Additionally, a grid-to-bond mapping layer is employed to project the grid-based stress field back onto each contact bond in the DEM simulation according to the position, which is feasible as there is at most one bond inserted in each grid. This ensures high-fidelity stress field prediction without redundant information aggregation.

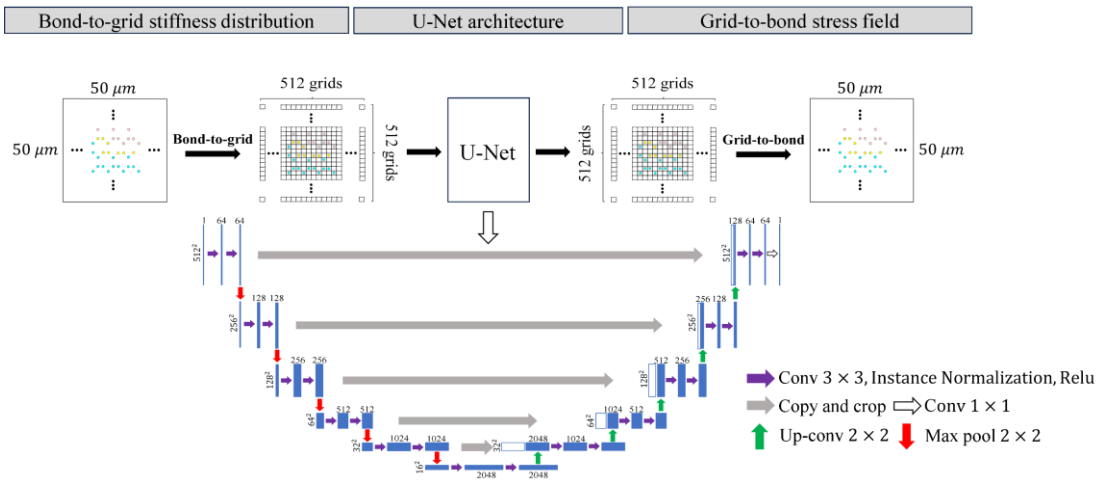

Fig. 4. Architecture of the proposed stress field prediction framework.

The training of weights in the designed U-Net model is carried out by minimizing the loss function, defined as the root mean squared error between the predicted and the DEM simulated stress distribution, which is defined as:

$$Loss_{rmse} = \sqrt{\frac{1}{NHW}\sum_{n=1}^{N}\sum_{i=1}^{H}\sum_{j=1}^{W}\left(\hat{\sigma}_{ij}^{n} - \sigma_{ij}^{n}\right)}. \quad (16)$$

where N is the number of samples in a batch, H and W denote the height and width of the spatial grid, respectively, $\hat{\sigma}$ is the DEM simulated stress field, and σ is the U-Net model predicted stress field. Meanwhile, a grid search method with five-fold cross-validation is employed in the data training process to select the best optimizer and the optimal network structure and parameters.

Finally, the detailed procedure for the proposed stress field prediction framework is presented as follows:

1: Define the target mapping from the lamina configuration M to the corresponding stress field $\sigma(x)$:

$$\sigma(x) = G(M)(x), \quad M = \{f^{f}, A, L\}. \quad (17)$$

2: Construct the input–output dataset using the calibrated DEM model, followed by a predefined preprocessing workflow:

$$k(x)^{\text{bond}} \xrightarrow{\text{preprocessing}} k(x)^{1\times512\times512}, \quad (18)$$

$$\sigma(x)^{\text{bond}} \xrightarrow{\text{preprocessing}} \sigma(x)^{1\times512\times512}. \quad (19)$$

3: Input the data into the appropriate U-Net model to approximate the defined mapping. The network architecture and training hyperparameters are determined through grid search coupled with cross-validation.

3. Results and discussion

3.1. Experiment setting

Datasets: In this work, four different fibre volume fractions are considered: 60%, which includes 44 circular fibres of radius 3.3 μm, 50%, which includes 37 circular fibres of radius 3.3 μm, 40%, which includes 30 circular fibres of radius 3.3 μm, and 30%, which includes 22 circular fibres of radius 3.3 μm (as shown in Fig. 5(a-d)). The

geometry and stress data from the generated RVE samples are divided into the training and testing subsets, as shown in Fig. 6, where 60% and 40% fibre volume fraction samples are combined to train the U-Net model, and the data from the RVEs with 30%, 40%, 50% and 60% fibre volume fractions are used for testing. This approach not only explores the U-Net model's ability to predict stress fields for RVEs with fibre volume fractions present in the training set but also investigates its applicability to RVEs with fibre volume fractions not seen during training. Specifically, predictions for RVEs with fibre volume fractions of 50% and 30% correspond to interpolation and extrapolation cases, respectively, which lie within and outside the range defined by the training data. Meanwhile, the typical stress-strain curve of the UD FRP composite laminae under transverse tension loads is shown in Fig. 5(e), which can be divided into an elastic linear regime and a plastic nonlinear regime. In this work, the U-Net model is used to predict the stress fields of the RVEs with the four different fibre volume fractions for both the elastic linear regime at the strain of 0.05% (Stage I) and the plastic nonlinear regime up to the timestep just before the first crack occurs (Stage II) to further understand its prediction ability. It should be noted that, in the following results, the normal bond force component is selected as the evaluation target, since it dominates material strength and failure in the discrete element framework.

Based on the above analysis, a total of 100 RVEs with 40% fibre volume fraction, 100 RVEs with 60% fibre volume fraction, 50 RVEs with 30% fibre volume fraction, and 50 RVEs with 50% fibre volume fraction are simulated to map the microstructure to the stress field in both linear and nonlinear regimes. Out of the simulation results, a random selection of 50 RVEs with 40% fibre volume fraction and 50 RVEs with 60% fibre volume fraction are combined to form the training dataset, while the remaining 50 RVEs for each fibre volume fraction are used as the testing dataset (as illustrated in Fig. 6).

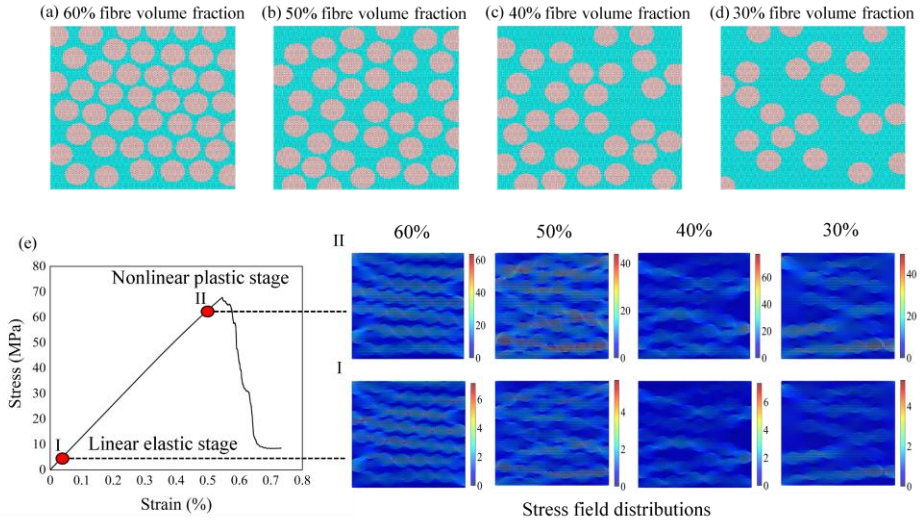

Fig. 5. (a) RVE with 60% fibre volume fraction. (b) RVE with 50% fibre volume fraction. (c) RVE with 40% fibre volume fraction. (d) RVE with 30% fibre volume fraction (e) The macroscopic stress-strain curve of a RVE sample under transverse tension loads, with stress field distributions at the selected linear elastic stage I corresponds to the strain of 0.05% and the nonlinear plastic stage II corresponds to the timestep before the first crack occurs of the four types of RVEs with 60%, 50%, 40%, and 30% fibre volume fractions.

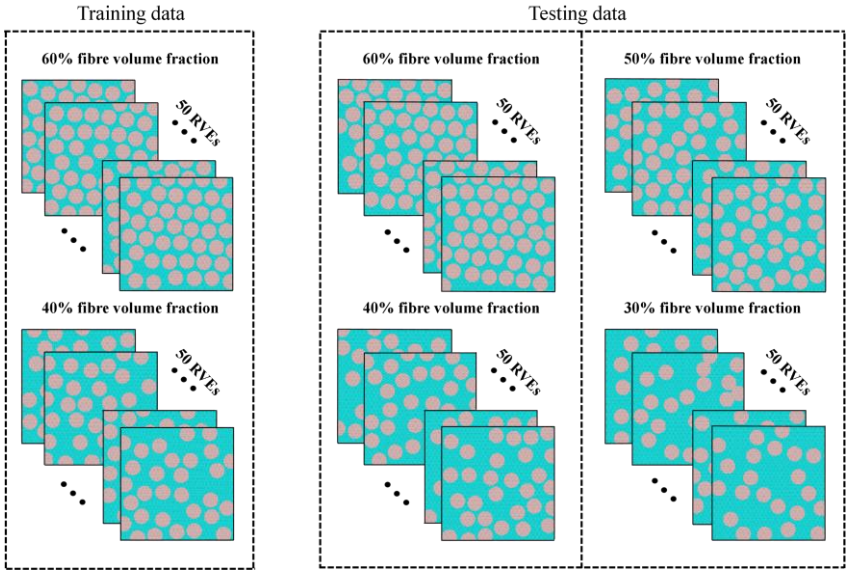

Fig. 6. Composition of the training and testing datasets.

1 Implementation details: To select the best optimizer and hyperparameters, the training

dataset is randomly divided into 5 subsets, each containing 10 RVEs with 40% fibre volume fraction and 10 RVEs with 60% fibre volume fraction, for five-fold cross-validation. Based on the cross-validation results, the Adam optimizer is used with a learning rate of 0.001, and training is conducted for 250 epochs with a batch size of 1 for both the linear and nonlinear stress field distribution prediction models. Fig. 7 and Fig. 8 show the evolution of the training and validation loss for the two models during the training process for each fold under the given training setup. It can be observed that, as training proceeds, the validation loss converges to a stable level without exhibiting a rebound or increasing trend, suggesting that no overfitting occurs and that the models exhibit robust generalization capability. Meanwhile, considering the slight divergence between the training and validation loss in the later stages of training, additional experiments based on an early-stopping strategy have been conducted. The results show that the model trained for 250 epochs achieves better performance on the test set, further supporting the effectiveness of the training setup determined through five-fold cross-validation.

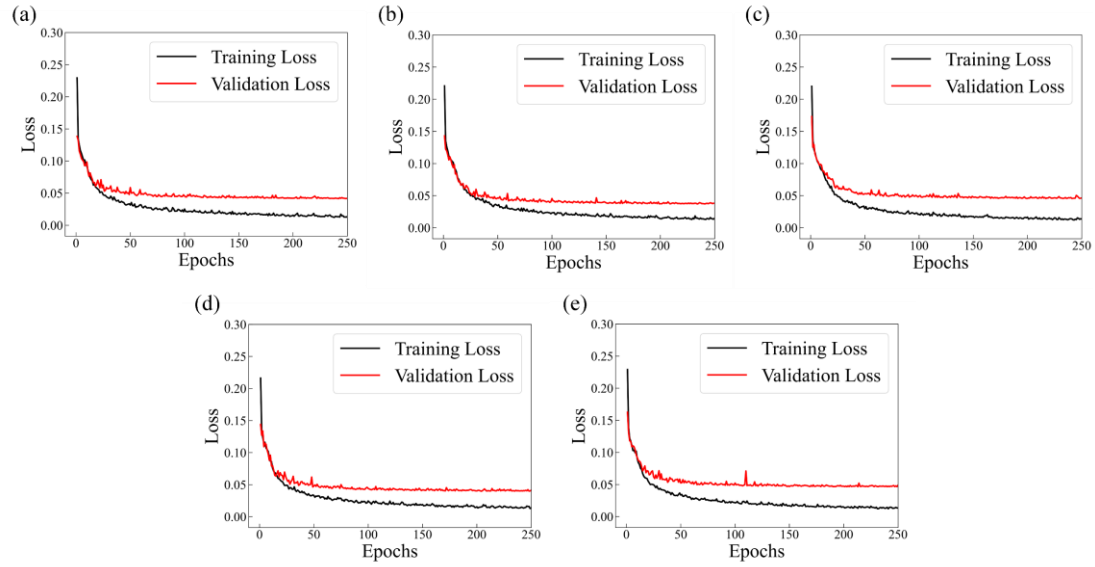

Fig. 7. The evolution of the training and validation loss for the linear stress field distribution prediction model during the training process in five-fold cross-validation: (a) Fold 1; (b) Fold 2; (c) Fold 3; (d) Fold 4; (e) Fold 5.

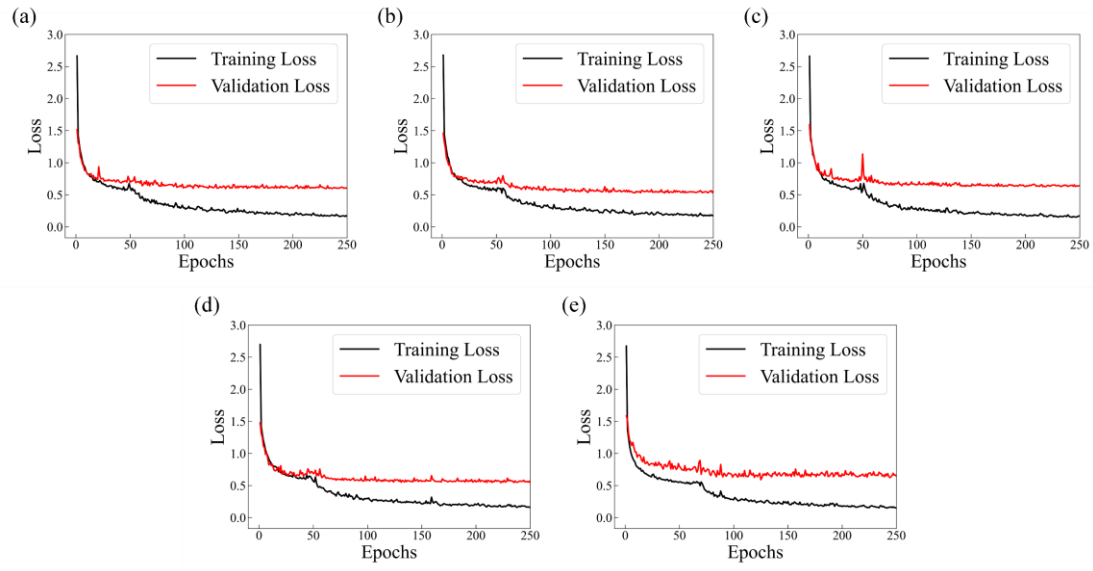

Fig. 8. The evolution of the training and validation loss for the nonlinear stress field distribution prediction model during the training process in five-fold cross-validation: (a) Fold 1; (b) Fold 2; (c) Fold 3; (d) Fold 4; (e) Fold 5.

The proposed U-Net models significantly improve the computational efficiency in comparison to the DEM simulation. For the nonlinear stress field analysis, the DEM model takes around 6 min per case. After a training time of 152 min, the trained U-Net model is capable of producing full-field stress predictions within 0.72 s on a standard laptop CPU (Intel i9-13900HX, 16GB RAM). When deployed on the GPU (NVIDIA RTX 4070), the inference time reduces to 0.09 s per analysis, which corresponds to a computational speedup exceeding 4000×. Meanwhile, the peak GPU memory usage during training and inference for the nonlinear stress field predictions is 3.181 GB and 2.764 GB, respectively, which are well within the capacity of standard consumer-grade GPUs, supporting the scalability and practical deployability of the proposed surrogate model, including its potential extension to larger or three-dimensional RVEs.

3.2. Stress field predictions for laminae with 60% and 40% fibre volume fractions

This section assesses the accuracy of the U-Net model in mapping from microstructures of lamina RVEs, which have the same fibre volume fractions as those in the training data but differ in fibre spatial distributions, to their corresponding linear and nonlinear stress fields. First, a random RVE sample from the 50 test samples with 60% fibre volume fraction is selected, and the true (DEM simulated) and predicted (U-Net model learned) stress fields of the sample are shown in Fig. 9(a-b). From these results, the absolute difference and correlation between them are calculated, and the corresponding error maps and correlation plots are presented in Fig. 9(c-d). Based on the prediction results, the true and predicted average forces, defined as the mean of all contact bond forces within the RVE, are calculated to be 0.89 N and 0.91 N, respectively, for the linear elastic stage at the strain of 0.05%. For the nonlinear plastic stage up to the timestep just before the first crack occurs, they are 8.69 N and 8.60 N. The relative errors, calculated as 1.57% for the prediction at the linear stage and 1.08% for the prediction at the nonlinear stage, indicate a close agreement between the prediction and the ground truth in terms of stress field distribution. In addition, the coefficient of determination (R^2) is used as an indicator to evaluate the model's performance in predicting the stress field distribution. As shown in the correlation plots in Fig. 9(d), the stress data at nearly all contact bonds are tightly clustered around y = x for both the linear and nonlinear stress field predictions, where high R^2 values of 0.9964 and 0.9957 are achieved, respectively. It can be observed that the R^2 value of the stress field prediction in the nonlinear stage slightly decreases compared to that in the linear stage, which can be attributed to the more heterogeneous and non-uniform stress distribution caused by plasticity-induced stress localization and redistribution.

To comprehensively evaluate the accuracy and effectiveness of the U-Net model, Fig. 9(e) presents the R^2 distributions across all 50 test samples with 60% fibre volume fraction. The mean R^2 values for the linear and nonlinear stress field predictions are 0.9922 and 0.9873, respectively, which are depicted by the vertical lines in Fig. 9(e). The high mean R^2 values suggest that the predictive model for both the linear and

nonlinear stress fields has strong generalization ability in dealing with samples with random fibre distributions. The standard deviations of the R^2 distributions are calculated as 0.0023 for the linear stage and 0.0067 for the nonlinear stage, supporting the earlier observation that the linear stress field prediction is more stable and reliable compared to the prediction during stages with increased material nonlinearity.

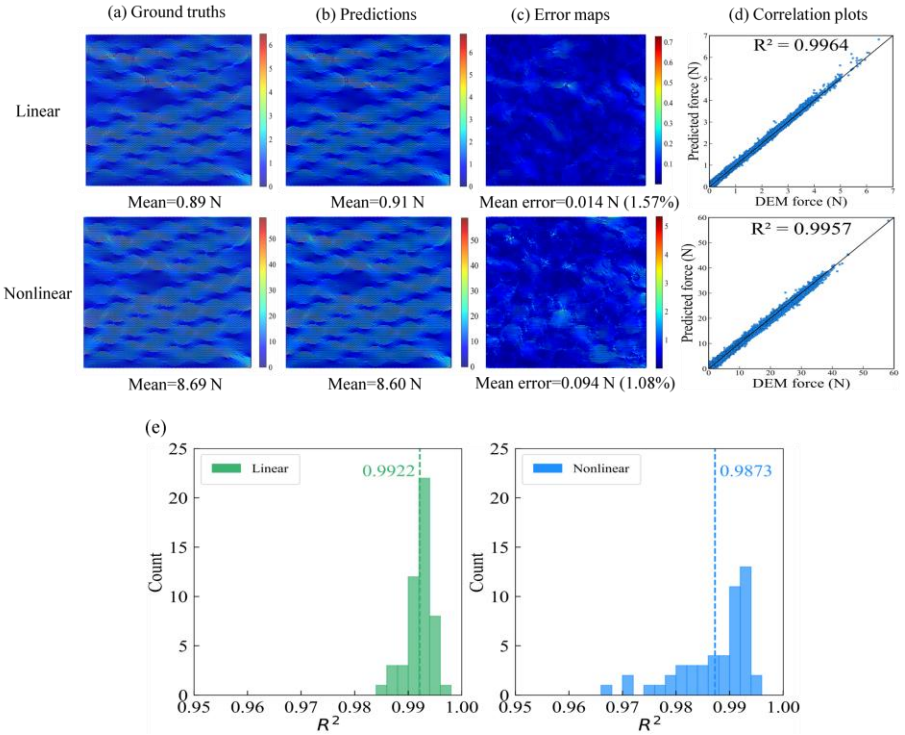

Fig. 9. The performance of the U-Net model in predicting the linear and nonlinear stress field distributions of RVEs with 60% fibre volume fraction. (a) True linear and nonlinear stress distributions. (b) Predicted linear and nonlinear stress distributions. (c) Error maps for the linear and nonlinear stress field distribution predictions. (d) Prediction-Simulation correlation plots for the linear and nonlinear stress field distributions. (e) R^2 distributions across 50 test samples for the linear and nonlinear stress field distribution predictions.

Similar to the performance assessment of the U-Net model on the RVE samples with 60% fibre volume fraction, its prediction ability on the 40% fibre volume fraction lamina RVEs is investigated. For a randomly selected RVE sample, the true stress fields, predicted stress fields, error maps and correlation plots are shown in Fig. 10(a-d), where

the relative errors for the prediction of the linear and nonlinear average forces are 0.52% and 3.66%, respectively, and the R^2 values are 0.9917 for the linear stress field prediction and 0.9906 for the nonlinear stress field prediction. For the entire dataset of 50 testing RVEs with 40% fibre volume fraction, as shown in Fig. 10(e), the model achieves high mean R^2 values for both the linear and nonlinear stress field predictions of samples with randomly distributed fibres, which are 0.9852 and 0.9753, respectively. Based on the evaluation metrics obtained, the model demonstrates strong capability in predicting both linear and nonlinear stress field distributions for samples with 40% fibre volume fraction. This further illustrates the model's effectiveness in mapping from the sample's microstructure to the corresponding stress field when dealing with lamina RVEs that have the same fibre volume fractions as those in the training data but different fibre spatial distribution patterns. Meanwhile, it can be noticed that as the fibre volume fraction decreases from 60% to 40%, the prediction accuracy is slightly reduced, which is mainly a consequence of the increasing randomness in fibre spatial distribution, thereby weakening the spatial correlations captured during training and posing greater challenges for the prediction task.

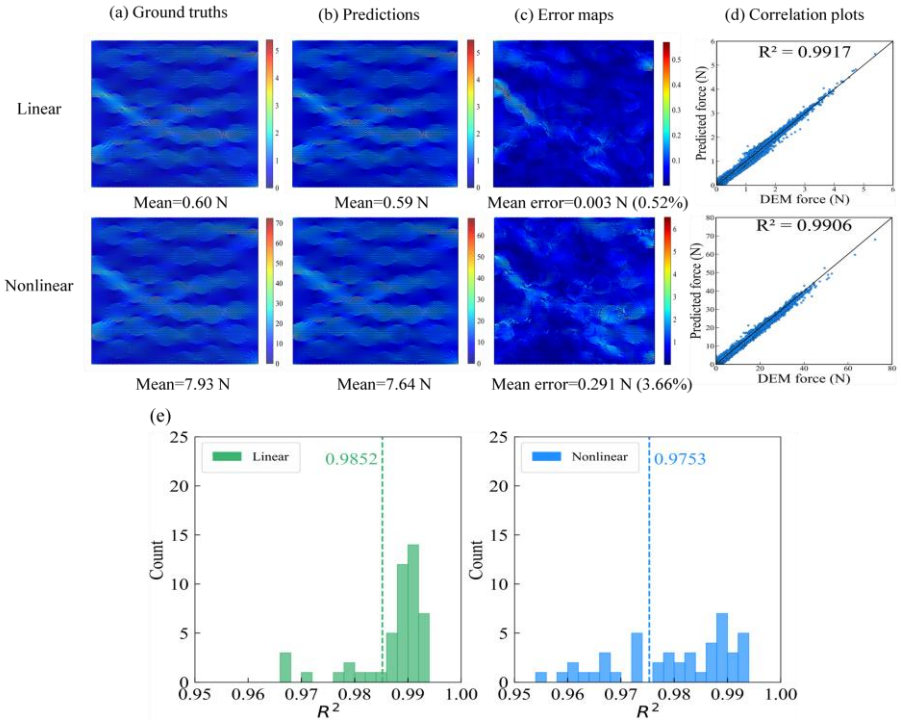

Fig. 10. The performance of the U-Net model in predicting the linear and nonlinear stress field distributions of RVEs with 40% fibre volume fraction. (a) True linear and nonlinear stress distributions. (b) Predicted linear and nonlinear stress distributions. (c) Error maps for the linear and nonlinear stress field distribution predictions. (d) Prediction-Simulation correlation plots for the linear and nonlinear stress field distributions. (e) R^2 distributions across 50 test samples for the linear and nonlinear stress field distribution predictions.

3.3. Stress field predictions for laminae with 50% and 30% fibre volume fractions

In this section, the effectiveness of the U-Net model in predicting the stress fields of the testing samples with both variations in fibre volume fraction and fibre spatial distribution is examined. For the testing samples, the change in fibre volume fraction introduces additional statistical features of samples' microstructures, which pose challenges to predictive models that lack physically meaningful information. In this work, the U-Net model is trained on DEM-generated data in which the composite microstructures are encoded using stiffness values of contact bonds, which preserves the physical meaning and consistency between the input microstructure and the resulting stress field distribution. The model is trained on lamina RVEs with 60% and 40% fibre volume fractions, and shows strong generalization ability for samples with 50% and 30% fibre volume fractions, which lie within and outside the interpolation range defined by the training data, respectively. Fig. 11(a-d) show the true stress maps, predicted stress maps, error maps and correlation plots for a sample randomly selected from the 50% fibre volume fraction RVEs. From these results, the relative errors for the prediction of the linear and nonlinear average forces are calculated as 1.78% and 1.16%, respectively, and the R^2 values are 0.9932 for the linear stress field prediction and 0.9926 for the nonlinear stress field prediction. Fig. 11(e) presents the R^2 distributions across all the 50 RVEs in the test dataset, where the mean R^2 values are calculated as 0.9850 and 0.9773 for the linear and nonlinear stress field predictions, respectively.

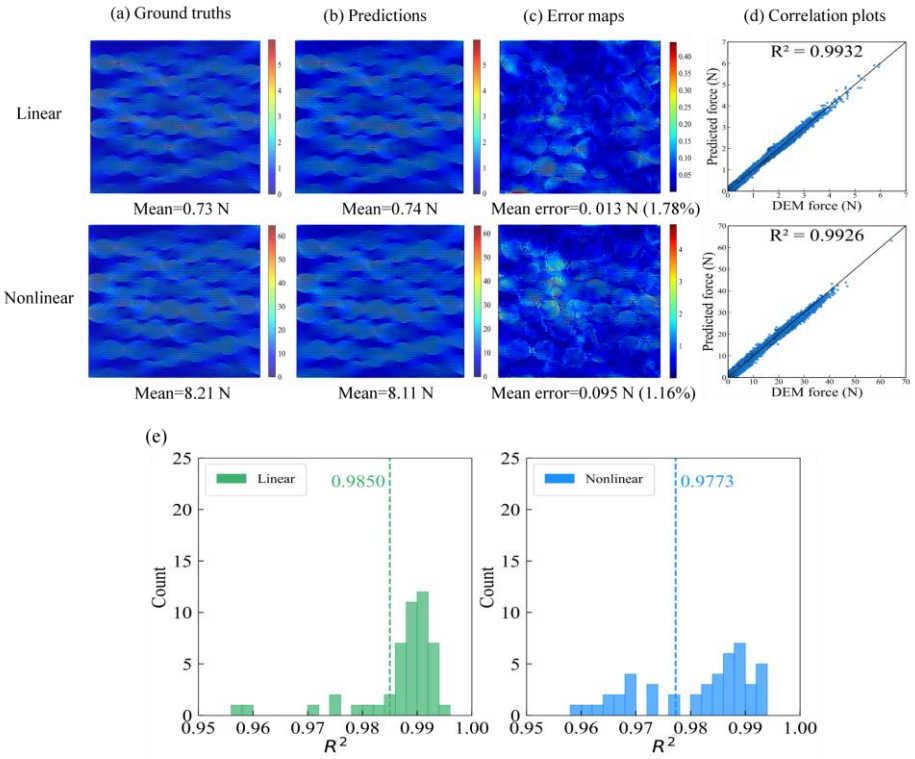

Fig. 11. The performance of the U-Net model in predicting the linear and nonlinear stress field distributions of RVEs with 50% fibre volume fraction. (a) True linear and nonlinear stress distributions. (b) Predicted linear and nonlinear stress distributions. (c) Error maps for the linear and nonlinear stress field distribution predictions. (d) Prediction-Simulation correlation plots for the linear and nonlinear stress field distributions. (e) R^2 distributions across 50 test samples for the linear and nonlinear stress field distribution predictions.

For a randomly selected sample with 30% fibre volume fraction, the true and predicted stress maps, error maps, and correlation plots are shown in Fig. 12(a-d). The R^2 distributions across all the 30% fibre volume fraction testing samples are presented in Fig. 12(e). It can be obtained that the relative errors in predicting the average forces are 3.16% and 4.57% for the linear and nonlinear stages, respectively, while the R^2 values for the prediction of stress fields are 0.9855 and 0.9847. The mean R^2 values across the entire test set are 0.9813 for the linear stress field prediction and 0.9765 for the nonlinear stress field prediction.

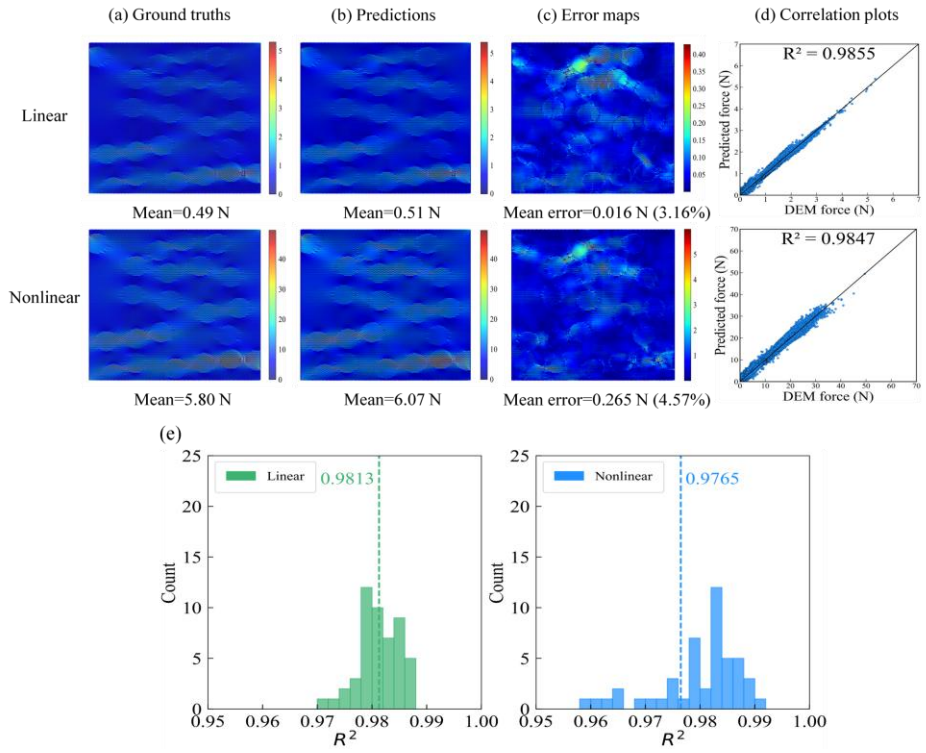

Fig. 12. The performance of the U-Net model in predicting the linear and nonlinear stress field distributions of RVEs with 30% fibre volume fraction. (a) True linear and nonlinear stress distributions. (b) Predicted linear and nonlinear stress distributions. (c) Error maps for the linear and nonlinear stress field distribution predictions. (d) Prediction-Simulation correlation plots for the linear and nonlinear stress field distributions. (e) R^2 distributions across 50 test samples for the linear and nonlinear stress field distribution predictions.

Since the weights and biases of the neural network are randomly initialized at the beginning of each training, different initial states may lead to variations in prediction performance and thus introduce uncertainty into the results. To enhance the reliability of the model, the U-Net model is trained using 10 different initial states. The prediction performance for RVEs with fibre volume fractions of 30% and 50%, which are not seen during training, is summarized in Table 2. As can be seen, the model exhibits good stability across different initial states. In particular, for the extrapolated case with 30% fibre volume fraction, the mean R^2 values remain at 0.9823 (95% confidence interval (CI), 0.9805–0.9842) and 0.9768 (95% CI, 0.9743–0.9792) for the linear and nonlinear

stress field predictions, respectively.

Table 2: Prediction performance of the U-Net model across 10 random initializations

Fibre volume fraction (%)	Regime	R^2	95% CI
30	Linear elasic	0.9823	[0.9805, 0.9842]
	Nonlinear plastic	0.9768	[0.9743, 0.9792]
50	Linear elastic	0.9852	[0.9832, 0.9871]
	Nonlinear plastic	0.9776	[0.9756, 0.9797]

To better demonstrate the generalization capability of the proposed prediction framework, a U-Net model is trained using only 100 DEM-generated RVEs with 60% fiber volume fraction. The prediction performance for RVEs with fiber volume fractions of 30%, 40%, 50%, and 60%, quantified by the mean R^2 values across 50 testing samples, is presented in Table 3. It can be seen that the model achieves the best prediction performance on testing samples with a fiber volume fraction of 60%, with the mean R^2 values of 0.9944 and 0.9909 for the linear and nonlinear stress fields, respectively. The lowest prediction accuracy is observed at 30% fiber volume fraction, where the corresponding mean R^2 values decrease to 0.9145 and 0.9057. It can be noticed that the prediction performance deteriorates from the model trained using DEM-generated samples with 60% and 40% fibre volume fractions, due to the reduced variability in microstructural configurations represented in the training data. Nevertheless, the mean R^2 values still exceed 0.9, demonstrating that the model maintains relatively high prediction accuracy.

Table 3: Prediction performance of the U-Net model trained on RVEs with 60% fibre volume fraction.

Fibre volume fraction (%)	R^2 in linear regime	R^2 in nonlinear regime
30	0.9145	0.9057
40	0.9250	0.9149
50	0.9581	0.9471

60	0.9944	0.9909

3.4. Comparison with U-Net trained on FEM-generated data

To further assess the robustness of the proposed prediction framework, a comparative study is performed to evaluate the performance of the U-Net model in predicting the linear and nonlinear stress field distributions trained on FEM-generated and DEM-generated data, respectively. In both cases, the training and testing data composition and training strategy are kept identical to ensure a rigorous and fair comparison. Specifically, the training data consists of 50 RVEs with 40% fibre volume fraction and 50 RVEs with 60% fibre volume fraction, and testing is conducted using an independent set of 50 RVEs at each fibre volume fraction of 30%, 40%, 50%, and 60%. As Fig. 13 shows, the U-Net model trained on FEM-generated data exhibits satisfactory performance on the testing data with a fiber volume fraction of 60%. However, as the fiber volume fraction decreases, the randomness of the microstructures increases. The prediction accuracy for both linear and nonlinear stress fields drop sharply, yielding R^2 values of only 0.5115 and 0.5073, respectively. In contrast, the U-Net model trained on DEM-generated data demonstrates consistently superior performance across fiber volume fractions included in the training set (60% and 40%) as well as those unseen during training (50% and 30%). The R^2 values for both linear and nonlinear stress field predictions all exceed 0.97.

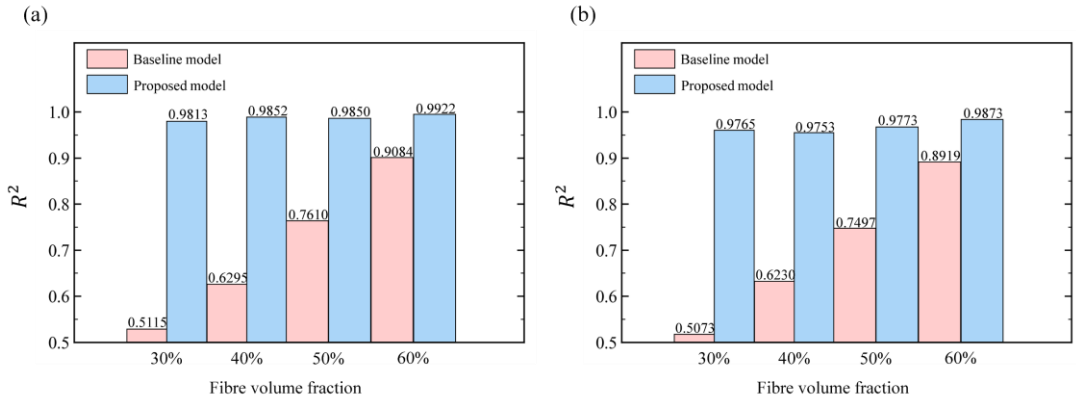

Fig. 13. Comparison of the proposed model and the U-Net trained on FEM-generated data for stress field predictions under different fibre volume fractions in

(a) linear and (b) nonlinear regime.

4. Conclusions

In this paper, a CNN-based U-Net model trained on DEM-generated data is developed to predict linear and nonlinear stress field distributions of UD FRP composite laminae. By mapping the stiffness distribution of a lamina directly to its corresponding stress field, the model is more effectively guided by the underlying physical knowledge during training, rather than relying on FEM-generated pixel-based binary image representations. The data for training and testing are generated by a validated RVE-based DEM model, and it is shown that the particle-based data structure from DEM simulations is highly compatible with the architecture of CNN-based models, which excel at extracting local dependencies due to their local perception and sub-sampling strategies. Based on the prediction results, the following conclusions are drawn up:

(1) To the authors' best knowledge, the integration of the U-Net model with DEM simulations achieves higher accuracy than existing studies in predicting linear and nonlinear stress fields of composite laminae which have the same fibre volume fractions but different fibre spatial distributions to the training samples. For the 60% and 40% fibre volume fractions laminae considered in this work, the mean R^2 values for the stress field prediction in the linear stage are 0.9922 and 0.9852, while in the nonlinear stage, they are 0.9873 and 0.9753, respectively.

(2) Trained on DEM-generated data, the U-Net model demonstrates strong generalization and extrapolation capabilities. This is, to our knowledge, the first attempt that a deep learning model can successfully predict the stress fields over samples which introduce variability in both fibre volume fraction and spatial distribution. For the 50% fibre volume fraction laminae, which lies within the interpolation range of the training samples, and the 30% fibre volume fraction laminae, which lies outside this range, the mean R^2 values for the stress field prediction in the linear stage are 0.9850 and 0.9813, while in the nonlinear stage, they are 0.9773 and 0.9765, respectively.

(3) The U-Net model trained on DEM-generated data significantly reduces the amount of training data required for the prediction of the linear and nonlinear stress fields. Only 100 lamina RVEs are used for training in this work and satisfactory prediction accuracy is made, whereas comparable models in literature typically rely on several hundred to thousands of training samples to achieve similar or even lower accuracy levels.

Based on the findings of this paper, the proposed model could be extended to the prediction of composite laminae with different microstructural configurations, such as the laminae containing fibre-rich and matrix-rich regions. Furthermore, future investigations could explore the prediction of damage initiation and propagation in composite laminae. As nonlinearity becomes more pronounced, additional deep learning approaches, including CNN-based, GAN-based, and sequence-based models, could be considered.

Meanwhile, beyond the current 2D plane strain scenario under transverse tension loads, the model could be extended to 3D and multi-axial loading conditions by incorporating the corresponding DEM simulation data into the training process. Such extensions would greatly enhance the capabilities of the surrogate analysis and offer deeper insights into the mechanical properties of the material.

CRediT authorship contribution statement

Siyu Zhao: Methodology, Investigation, Data curation, Formal analysis, Software, Writing - Original Draft; **Xiaoxuan Ding:** Methodology, Software, Writing - Review & Editing; **Jianqiao Ye:** Supervision, Writing - Review & Editing; **Xiaonan Hou:** Conceptualization, Methodology, Project administration, Supervision, Writing - Review & Editing.

Date availability

Data will be made available on request.

References

[1] P. Xiang, A.S. Ademiloye, H. Wang, et al. Static and dynamic performance analysis of structures and materials under complex loads and environmental excitation, Front. Mater. 12 (2025) 1620625.

[2] A. Lounis, A. Attia, A.A. Bousahla, et al. Effect of viscoelastic Foundation on the dynamic analysis of FG polymer nanoplates reinforced with graphene nanoplatelets, Adv. Nano Res. 19 (1) (2025) 29-39.

[3] A.A. Bousahla, H. Bellifa, A. Tounsi, et al. Enhancing analysis of cross-ply laminated composite plates: A simplified approach for flexural and stability evaluation, Eurasia. Proc. Sci. Technol. Eng. Math. 32 (2024) 93-100.

[4] A.A. Bousahla, Free Vibration Analysis of Functionally Graded Plates on Viscoelastic Foundations, in: Vibration Engineering - Analysis, Control, and Utilization, IntechOpen, 2025.

[5] A. Kadiri, M. Bendaida, A. Attia, et al. Wave propagation in FG polymer composite nanoplates embedded in variable elastic medium, Adv. Nano Res. 17 (3) (2024) 235-248.

[6] A. Remil, K.H. Benrahou, K. Draiche, et al. A simple HSDT for bending, buckling and dynamic behavior of laminated composite plates, Struct. Eng. Mech. 70 (3) (2019) 325-337.

[7] A. Attia, A.T. Berrabah, F. Bourada, et al. Free vibration analysis of thick laminated composite shells using analytical and finite element method, J. Vib. Eng. Technol. 12 (7) (2024) 7711-7728.

[8] H.C. Dewangan, S.K. Panda, N. Sharma, A review of linear and nonlinear structural responses of laminated flat/curved panels with and without cutout under thermo-mechanical loading, Compos. Struct. 303 (2023) 116340.

[9] D. Thomson, M. Ploeckl, J. Hoffmann, et al. A review of the effect of loading rate on the mechanical properties of unidirectional carbon fibre reinforced polymer composites, Compos. A: Appl. Sci. Manuf. 193 (2025) 108773.

[10] J.N. Reddy, Mechanics of laminated composite plates and shells: theory and analysis, second ed., CRC press, 2000.

[11] E. Rashidinejad, H. Ahmadi, M. Hajikazemi, et al. Closed-form analytical solutions for predicting stress transfers and thermo-elastic properties of short fiber composites, Mech. Adv. Mater. Struct. 30 (23) (2023) 4731-4751.

[12] J.D. Mathias, X. Balandraud, M. Grédiac, Experimental investigation of composite patches with a full-field measurement method, Compos. A: Appl. Sci. Manuf. 37 (2) (2006) 177-190.

[13] M. Kashfuddoja, M. Ramji, Whole-field strain analysis and damage assessment of adhesively bonded patch repair of CFRP laminates using 3D-DIC and FEA, Compos. B: Eng. 53 (2013) 46-61.

[14] F. Rastellini, S. Oller, O. Salomón, et al. Composite materials non-linear modelling for long fibre-reinforced laminates: Continuum basis, computational aspects and validations, Comput. Struct. 86 (9) (2008) 879-896.

[15] Y. Qian, Z. Li, X. Zhou, et al. The strength prediction model of unidirectional fiber reinforced composites based on the renormalization group method, Compos. Sci. Technol. 253 (2024) 110639.

[16] L.T. Tenek, J. Argyris, Finite element analysis for composite structures, Springer Science & Business Media, 2013.

[17] J.N. Reddy, An Introduction to Nonlinear Finite Element Analysis: with applications to heat transfer, fluid mechanics, and solid mechanics, second ed., OUP Oxford, 2014.

[18] Y. Ismail, Y. Sheng, D. Yang, et al. Discrete element modelling of unidirectional fibre-reinforced polymers under transverse tension, Compos. B: Eng. 73 (2015) 118-125.

[19] F.E. Bock, R.C. Aydin, C.J. Cyron, et al. A review of the application of machine learning and data mining approaches in continuum materials mechanics, Front. Mater. 6 (2019) 110.

[20] L. Song, D. Wang, X. Liu, et al. Prediction of mechanical properties of composite materials using multimodal fusion learning, Sens. Actuators. A: Phys. 358 (2023) 114433.

[21] M. Mirkhalaf, I. Rocha, Micromechanics-based deep-learning for composites: Challenges and future perspectives, Eur. J. Mech. A. Solids. 105 (2024) 105242.

[22] Z. Gu, Y. Liu, D.J. Hughes, et al. A parametric study of adhesive bonded joints with composite material using black-box and grey-box machine learning methods: Deep neuron networks and genetic programming, Compos. B: Eng. 217 (2021) 108894.

[23] X. Ding, X. Hou, M. Xia, et al. Predictions of macroscopic mechanical properties and microscopic cracks of unidirectional fibre-reinforced polymer composites using deep neural network (DNN), Compos. Struct. 302 (2022) 116248.

[24] X. Ding, Z. Gu, X. Hou, et al. Effects of defects on the transverse mechanical response of unidirectional fibre-reinforced polymers: DEM simulation and deep learning prediction, Compos. Struct. 321 (2023) 117301.

[25] A. Cecen, H. Dai, Y.C. Yabansu, et al. Material structure-property linkages using three-dimensional convolutional neural networks, Acta Mater. 146 (2018) 76-84.

[26] M.V. Pathan, S.A. Ponnusami, J. Pathan, et al. Predictions of the mechanical properties of unidirectional fibre composites by supervised machine learning, Sci. Rep. 9 (1) (2019) 13964.

[27] M. Mozaffar, R. Bostanabad, W. Chen, et al. Deep learning predicts path-dependent plasticity, Proc. Natl. Acad. Sci. 116 (52) (2019) 26414-26420.

[28] G.X. Gu, C.T. Chen, M.J. Buehler, De novo composite design based on machine learning algorithm, Extreme Mech. Lett. 18 (2018) 19-28.

[29] Z. Yang, Y.C. Yabansu, R. Al-Bahrani, et al. Deep learning approaches for mining structure-property linkages in high contrast composites from simulation datasets, Comput. Mater. Sci. 151 (2018) 278-287.

[30] C. Rao, Y. Liu, Three-dimensional convolutional neural network (3D-CNN) for heterogeneous material homogenization, Comput. Mater. Sci. 184 (2020) 109850.

[31] C. Herriott, A.D. Spear, Predicting microstructure-dependent mechanical properties in additively manufactured metals with machine-and deep-learning methods, Comput. Mater. Sci. 175 (2020) 109599.
[32] B. Liu, N. Kovachki, Z. Li, et al. A learning-based multiscale method and its application to inelastic impact problems, J. Mech. Phys. Solids. 158 (2022) 104668.
[33] E. Champa-Bujaico, A.M. Díez-Pascual, A.L. Redondo, et al. Optimization of mechanical properties of multiscale hybrid polymer nanocomposites: A combination of experimental and machine learning techniques, Compos. B: Eng. 269 (2024) 111099.
[34] G. Zhao, T. Xu, X. Fu, et al. Machine-learning-assisted multiscale modeling strategy for predicting mechanical properties of carbon fiber reinforced polymers, Compos. Sci. Technol. 248 (2024) 110455.
[35] L. Liang, M. Liu, C. Martin, et al. A deep learning approach to estimate stress distribution: a fast and accurate surrogate of finite-element analysis, J. R. Soc. Interface. 15 (138) (2018) 20170844.
[36] E. Haghighat, M. Raissi, A. Moure, et al. A physics-informed deep learning framework for inversion and surrogate modeling in solid mechanics, Comput. Methods Appl. Mech. Eng. 379 (2021) 113741.
[37] M. Maurizi, C. Gao, F. Berto, Predicting stress, strain and deformation fields in materials and structures with graph neural networks, Sci. Rep. 12 (1) (2022) 21834.
[38] J.R. Mianroodi, N.H. Siboni, D. Raabe, Teaching solid mechanics to artificial intelligence—a fast solver for heterogeneous materials, npj Comput. Mater. 7 (1) (2021) 99.
[39] H. Jiang, Z. Nie, R. Yeo, et al. Stressgan: A generative deep learning model for two-dimensional stress distribution prediction, J. Appl. Mech. 88 (5) (2021) 051005.
[40] Z. Nie, H. Jiang, L.B. Kara, Stress field prediction in cantilevered structures using convolutional neural networks, J. Comput. Inf. Sci. Eng. 20 (1) (2020) 011002.
[41] A. Frankel, K. Tachida, R. Jones, Prediction of the evolution of the stress field of polycrystals undergoing elastic-plastic deformation with a hybrid neural network model, Mach. Learn.: Sci. Technol. 1 (3) (2020) 035005.

[42] P.M. Khanolkar, C.C. McComb, S. Basu, Predicting elastic strain fields in defective microstructures using image colorization algorithms, Comput. Mater. Sci. 186 (2021) 110068.

[43] B.P. Croom, M. Berkson, R.K. Mueller, et al. Deep learning prediction of stress fields in additively manufactured metals with intricate defect networks, Mech. Mater. 165 (2022) 104191.

[44] H. Feng, P. Prabhakar, Difference-based deep learning framework for stress predictions in heterogeneous media, Compos. Struct. 269 (2021) 113957.

[45] Z. Yang, C.H. Yu, K. Guo, et al. End-to-end deep learning method to predict complete strain and stress tensors for complex hierarchical composite microstructures, J. Mech. Phys. Solids. 154 (2021) 104506.

[46] A. Bhaduri, A. Gupta, L. Graham-Brady, Stress field prediction in fiber-reinforced composite materials using a deep learning approach, Compos. B: Eng. 238 (2022) 109879.

[47] X. Peng, Q. Yao, B. Yi, et al. Deep learning approach for predicting multi-component stress fields in fiber-reinforced composites under different load paths, Compos. Sci. Technol. 267 (2025) 111198.

[48] M. Li, Y. Zhang, W. Qu, et al. A triplet attention-enhanced deep learning approach to predict full-field stress of unidirectional CFRP composites with microvoids, Compos. Sci. Technol. 271 (2025) 111361.

[49] S. Wang, T.R. Liu, S. Sankaran, et al. Micrometer: Micromechanics transformer for predicting full field mechanical responses of heterogeneous materials, Comput. Methods Appl. Mech. Eng. 448 (2026) 118373.

[50] P. Zhang, Y. Xiang, K. Tang, Deep learning surrogate for phase field modeling in fiber-reinforced composites: From stress evolution to final crack path, Comput. Methods Appl. Mech. Eng. 448 (2026) 118518.

[51] Q. Xu, Z. Nie, H. Xu, et al. SuperMeshing: A New Deep Learning Architecture for Increasing the Mesh Density of Metal Forming Stress Field With Attention Mechanism And Perceptual Features, in: ASME 2021 International Design Engineering Technical

Conferences and Computers and Information in Engineering Conference, 2021, Paper No. V03BT03A041.

[52] M. Yacouti, M. Shakiba, Integrated convolutional and graph neural networks for predicting mechanical fields in composite microstructures, Compos. A: Appl. Sci. Manuf. 190 (2025) 108618.

[53] R. Sepasdar, A deep learning approach to predict full-field stress distribution in composite materials, Virginia Tech, 2021.

[54] R. Sepasdar, A. Karpatne, M. Shakiba, A data-driven approach to full-field nonlinear stress distribution and failure pattern prediction in composites using deep learning, Comput. Methods Appl. Mech. Eng. 397 (2022) 115126.

[55] D. Yang, J. Ye, Y. Tan, et al. Modeling progressive delamination of laminated composites by discrete element method, Comput. Mater. Sci. 50 (3) (2011) 858-864.

[56] D. Yang, Y. Sheng, J. Ye, et al. Dynamic simulation of crack initiation and propagation in cross-ply laminates by DEM, Compos. Sci. Technol. 71 (11) (2011) 1410-1418.

[57] Y. Ismail, D. Yang, J. Ye, Discrete element method for generating random fibre distributions in micromechanical models of fibre reinforced composite laminates, Compos. B: Eng. 90 (2016) 485-492.

[58] Itasca Consulting Group Inc, PFC - Particle Flow Code, Ver. 6.0, Minneapolis, 2019.

[59] P.D. Soden, M.J. Hinton, A.S. Kaddour, Lamina properties, lay-up configurations and loading conditions for a range of fibre reinforced composite laminates, in: Failure criteria in fibre-reinforced-polymer composites, 2004, pp. 30-51.

[60] R. Kačianauskas, V. Vadluga, Lattice-based six-spring discrete element model for discretisation problems of 2D isotropic and anisotropic solids, Mech. 76 (2) (2009) 11-19.

[61] Y. Ismail, D. Yang, J. Ye, A DEM model for visualising damage evolution and predicting failure envelope of composite laminae under biaxial loads, Compos. B: Eng. 102 (2016) 9-28.

[62] Y. Wang, F. Tonon, Calibration of a discrete element model for intact rock up to its peak strength, Int. J. Numer. Anal. Methods Geomech. 34 (5) (2010) 447-469.